Coupling of spin-wave modes in extended ferromagnetic thin film antidot arrays

S. McPhail, C. M. Gürtler, J. M. Shilton, N. J. Curson, and J. A. C. Bland
Cavendish Laboratory, University of Cambridge, Cambridge CB3 0HE, United Kingdom
(Received 5 October 2004; published 13 September 2005)

The pattern-induced frequency splitting of propagating spin-wave modes of extended micron scale square antidot arrays fabricated from 15–120-nm-thick $Ni_{80}Fe_{20}$ films has been studied via Brillouin light scattering. The splitting of the surface and first volume mode is observed to be of the order of 2 GHz. Using a simple model which assumes that the spectral weight of the scattered light directly reflects the map of the spatially varying demagnetizing field, the peak splitting can be explained satisfactorily. We infer that the measured spectrum is the result of almost uncoupled propagating spin waves which correspond to regions of near constant demagnetizing field within the unit cell of the array. We conclude that in contrast to confinement effects seen in small isolated structures (dots, rectangles), the local magnetization and demagnetizing field principally determine the spin-wave mode character *and* its dispersion with wave vector rather than the edge boundary conditions of the array structure.

DOI: 10.1103/PhysRevB.72.094414 PACS number(s): 75.30.Ds, 75.75.+a

I. INTRODUCTION

The GHz frequency magnetic-resonance properties of magnetic films are of increasing importance in magnetic information storage technologies.[1] Advances in lithography make it possible for well defined magnetic nanostructures to be studied, but until now most studies have focused on static magnetic properties. While the spin-wave modes of magnetic continuous films (of more than a few monolayers thickness) are well understood,[2–4] by contrast, the spin-wave modes of patterned films are not well understood and are a focus of current research.[5–10]

Patterning a magnetic film changes the properties of its spin-wave modes due to (i) the demagnetizing fields that exist in patterned structures, and (ii) the boundary conditions that the spin waves must satisfy at the edges of the pattern. For spin waves probed by Brillouin light scattering (BLS), both these effects become significant in films with pattern length scales of approximately a micron. Structures on these length scales can have demagnetizing fields comparable in strength to the typical experimentally applied fields of 10^4-10^5 Am^{-1}. Moreover, the use of visible light in BLS experiments implies that the wavelength of the spin waves observed is on the micron scale (the transferred wave vector $q_{\parallel}=0.4-2.1\times10^5$ cm^{-1}), thus the properties of the spin waves may be greatly altered by the boundary conditions at the edges of structures on this scale.

The boundary conditions for $Ni_{80}Fe_{20}$ films are usually assumed to be that the spin waves have antinodes at the surfaces of a structure. This is due to the very low surface anisotropy of $Ni_{80}Fe_{20}$ which implies that no surface pinning occurs. In wire and dot structures, the boundary conditions have been shown to cause spin-wave mode splitting.[5–10] $Ni_{80}Fe_{20}$ structures with thicknesses in the range 10–50 nm and $\sim$1-μm scale patterns were studied. The surface mode was found to split into three to four peaks with a separation of $\sim$1 GHz while no splitting in the first volume mode was observed, consistent with confinement induced splitting.

Recent investigations[8,9] of confined spin waves in micron scale elements (rectangles and dots) have shown that in these systems, the spin-wave modes are determined by a combination of localization effects and the inhomogeneous demagnetizing field causing a quantization of the surface mode splitting. However, the question arises as to what extent the boundary conditions influence the spin-wave frequencies present in antidot arrays where long-range propagation occurs. Antidot arrays have received only limited attention and to our knowledge all such studies to date have focused on Fe films only.[11–13] Antidot arrays provide a unique opportunity to study the effects of both long-range dipolar interaction and local confinement in one sample due to the extended nature of the structure. In particular, the periodicity of the structure is expected to lead to a periodic modulation of the demagnetizing field and might thus give rise to modulated or even new spin-wave modes.

In the present work we have investigated square hole antidot arrays with a cell size of 1×1 μm^2, much smaller than the coherence length expected for the spin waves. It is an open question as to how strongly spin waves in different parts of such a structure might interact, keeping in mind that the exchange interaction is unbroken throughout the sample.

II. EXPERIMENTAL METHOD

A 0.35-μm polymethyl methacrylate (PMMA) resist was spin coated onto a GaAs (100) substrate. The resist was exposed in patches using an *e*-beam raster scanned in the *y* and *z* directions (*x* is the out-of-plane direction) and developed to leave PMMA pillars. A nominal thickness of 120, 60, or 15 nm of $Ni_{80}Fe_{20}$ and 3 nm of Au was deposited in UHV by molecular beam epitaxy (MBE) using a $Ni_{80}Fe_{20}$ source. The $Ni_{80}Fe_{20}$ deposition rate was $\sim$0.4 nm/min. The growth took place at room temperature and at a maximum pressure of $\sim2\times10^{-9}$ mbar (from a base pressure of $\sim8\times10^{-10}$ mbar). The pillars were lifted off using acetone to leave an antidot array. The removal of the pillars was confirmed by scanning electron microscopy (SEM) and optical microscopy.

The lateral size of each patterned patch was 180×180 μm^2. One patch on each film contained continu-

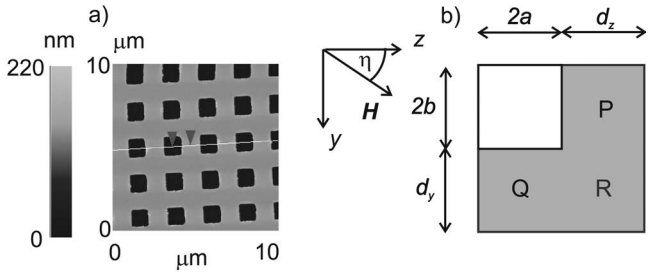

FIG. 1. (a) AFM picture of the $[(1,1),(1,1)]$-μm 120-nm array, (b) diagram of unit cell showing dimensions and significant points.

ous metal and the others contained arrays of square antidots with dimensions $[(2a,2b),(d_z,d_y)]$ as defined in Fig. 1(b). An atomic force microscopy (AFM) picture of the $[(1,1),(1,1)]$-μm array is shown in Fig. 1(a). The thickness values t of the magnetic layer of the three patterned samples were measured by AFM to be 118 ± 4, 59 ± 1, and 14 ± 1 nm, respectively. In each case the spacing between the antidots was the same as the sidelength of the antidots. η is defined to be the in-plane angle between the external field and the z axis of the array [see Fig. 1(b)]. The $\eta=0°$ direction is aligned with the GaAs $(0\bar{1}1)$ direction.

Longitudinal magneto-optical Kerr effect (MOKE) (with the angle between the incident beam and the surface normal $\phi\sim15°$) and BLS experiments both took place *ex situ*. BLS experiments were performed in the Voigt geometry: **H** in plane and perpendicular to the incident light. ϕ (defined as for the MOKE experiment) could be varied between 10° and 60°, i.e., $q_{\|}=(4\pi/\lambda_{\text{laser}})\sin\phi=0.4-2.1\times10^5$ cm^{-1}. The 514.5-nm line of an Ar^+ ion laser was used with an optical power at the sample surface of $\lesssim100$ mW. The scattered light was directed into a Sandercock 3+3 pass interferometer as described previously;[4] diffracted light was removed with a shaped stop.

III. EXPERIMENTAL RESULTS AND MODEL

The easy and hard axes of the 120-nm and 15-nm continuous film patches were located from the shape of the MOKE loops. Both films were uniaxial with an anisotropy constant K_U of $<2\times10^3$ Jm^{-3} (despite the fact that the films were not annealed) and a coercivity of $<4\times10^3$ Am^{-1} (50 Oe). This anisotropy did not lead to a measurable anisotropy in the BLS spectra. This lack of anisotropy also implies that there is little effect on the BLS spectra from the finite patch size.

The BLS results taken from continuous films were interpreted using the model of Ref. 4. For each continuous film the Landau-Lifshitz equation,

$$\frac{\partial\mathbf{M}}{\partial t}=-\frac{\mu_0 eg}{2m_e}\mathbf{M}\times\left[H_{\text{ex}}+\mathbf{H}_{\text{demag}}-\left(\frac{1}{\mu_0 M_s}\right)\nabla E_{\text{ani}}+\left(\frac{2A}{\mu_0 M_s^2}\right)\nabla^2\mathbf{M}\right] \quad (1)$$

(where A is the exchange stiffness, g the g factor, and M_s the saturation magnetization), was solved together with Maxwell's equations by the substitution of in-plane traveling-wave solutions which have the out-of-plane profile of sinusoidal standing waves (volume modes) or decaying exponentials (surface/Damon-Eshbach modes).[2,3] The magnetic properties of the material were calculated by an iterative method[4] from the frequencies of the spin waves as a function of external field.

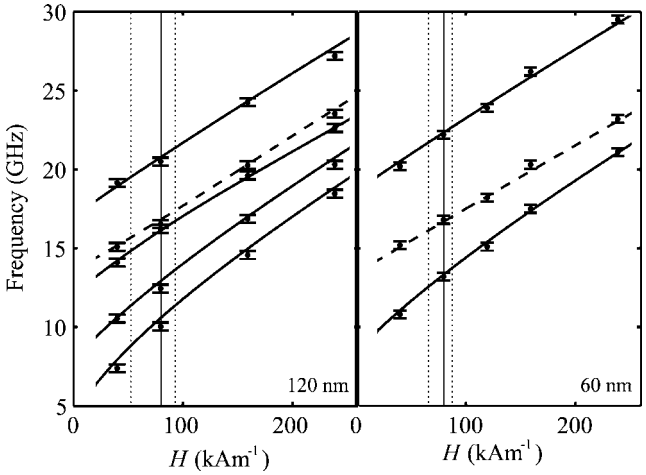

FIG. 2. Field dependence of surface (dashed line) and volume (solid line) modes for a 120-nm and 60-nm continuous $Ni_{80}Fe_{20}$ film obtained by solution of Eq. (1) with parameters as given in the text and $\phi=45°$. For comparison, the vertical lines mark the applied (solid line) and internal fields (dashed lines) in regions Q and R which give rise to the 120-nm $\eta=0°$ and $\eta=45°$ "antidot" spectra shown in Fig. 3.

Figure 2 shows the external field dependence of the surface and volume modes for both the 120- and 60-nm continuous film patches. The fit lines show predicted spin-wave mode frequencies for the best-fit parameters. For the 120-nm film these are $A=(8.57\pm0.15)\times10^{-12}$ Jm^{-1}, $g=2.14\pm0.03$, and $M_s=(7.13\pm0.08)\times10^5$ Am^{-1}. The spin waves of the 60- and 15-nm films were fitted simultaneously with $A=(9.02\pm0.07)\times10^{-12}$ Jm^{-1}, $g=2.14\pm0.03$, and $M_s=(7.06\pm0.05)\times10^5$ Am^{-1}.

Representative BLS spectra of continuous and patterned films are shown in Fig. 3. The dashed lines represent model spectra obtained from the simulation (described later on in detail). The peak frequencies were found by fitting the peaks with Lorentzian to the sixth power curves (the transmission function of the spectrometer).

The peaks in the spectrum of the 120-nm continuous film are replaced by double peaks in the corresponding 120-nm patterned film (see upper part of Fig. 3). This is most apparent for the Stokes surface mode and the anti-Stokes first volume mode (compare top two spectra in Fig. 3). The 60-nm structures (not shown here) were found to exhibit a similar peak splitting. However, it was less pronounced than in the 120-nm structures. The 15-nm structures, on the other hand, show little or no splitting for $\eta=0°$ (see lower part of Fig. 3). Nevertheless, the peaks appear to be asymmetric with a larger signal at low frequencies as is consistent with the observations by Zivieri *et al.*[14] The width of the peaks is increased from that of the continuous film.

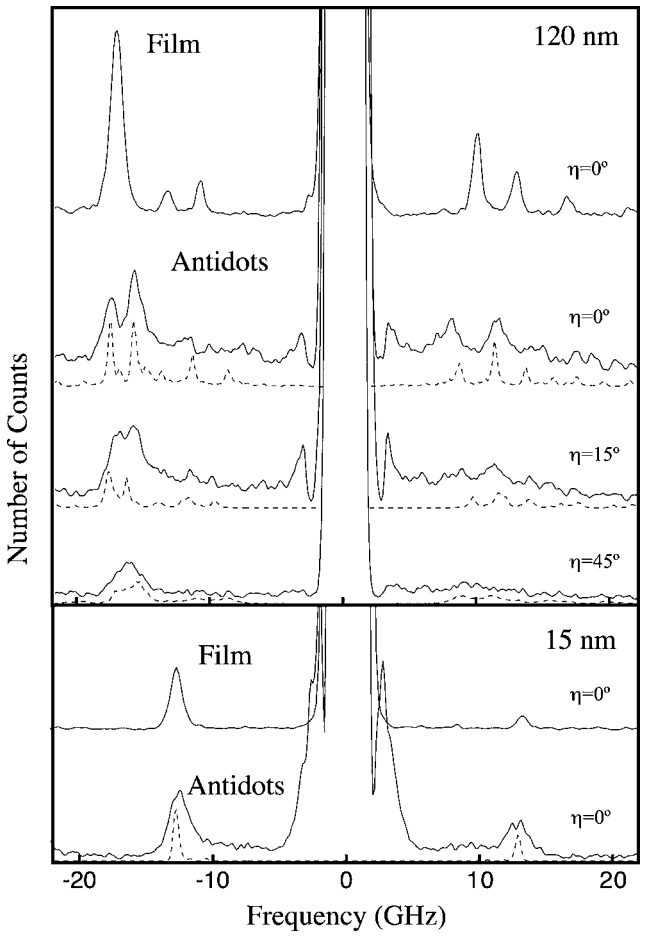

FIG. 3. Set of BLS spectra measured from continuous films and $[(1,1),(1,1)]$-μm antidot arrays in an applied field of $H=80$ kAm^{-1}. The dashed lines in these plots show the model prediction for the spectra.

In Fig. 4, the frequencies of the surface mode peaks of the 120-nm-thick film and structures are plotted as a function of $\phi(q_\parallel)$ and η (applied magnetic field direction). There, a monotonic increase of the frequency with ϕ can be seen which is consistent with the well-known dependence of the surface modes on the in-plane wave vector. Furthermore, the split peaks have a similar variation with ϕ when compared to the variation of the surface modes of the continuous films. This is in stark contrast to Refs. 6–10 where a dispersionless, quantized surface mode was seen. As in the continuous films there is no signature of the surface mode on the anti-Stokes side of the spectra. It is also worth noting that the volume modes are split by a larger amount than the surface modes,

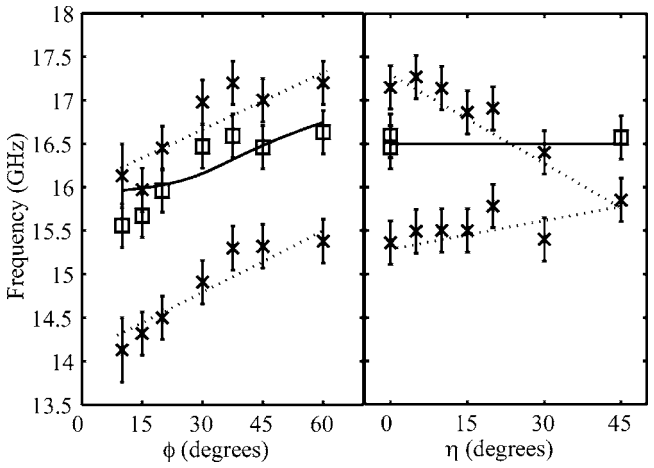

FIG. 4. Splitting of surface mode as function of $\phi(q_\parallel)$ and η (applied field direction) in the 120-nm-thick $[(1,1),(1,1)]$-μm structure with $H=80$ kAm^{-1}. □ are the continuous film surface mode, × are the two prominent peaks of the surface mode in the patterned film. The solid lines are plots of the solutions to Eq. (1) for the continuous film surface mode, the dotted lines are guides to the eye.

again in contrast to the confined structures of Refs. 6–10 where there was no observable splitting in the volume modes. The splitting of the modes can be seen to collapse as η approaches 45° (see relevant part of Fig. 3 and plot on the right of Fig. 4).

The "OOMMF" software package (version 1.1a2) (Ref. 15) was used to micromagnetically model the demagnetizing field of each structure, with each micromagnetic cell uniform in the x (out-of-plane) direction. The simulation was also limited in that the OOMMF package used did not support repeated boundary conditions (corresponding to an infinite antidot film), only finite structures. Arrays were simulated by modeling a structure of 5×5 unit cells and examining the central one. The computational cell size was fixed at 50 nm (so that each unit cell was 40×40 computational cells). No differences in the demagnetizing field or magnetization orientation could be seen between the central unit cell and those adjacent to it. The measured saturation magnetization and exchange were used, and the magnetocrystalline anisotropy was set to zero. Figures 5(a) and 5(c) show the component of the demagnetizing field parallel to the applied field for the 120- and 15-nm films at $\eta=0°$. Stationary points (at P, Q, and R) are surrounded by extended regions with similar field values. The demagnetizing field value is positive at Q and negative at P and R (with only a small difference between the field at the two latter points). A similar spatial variation

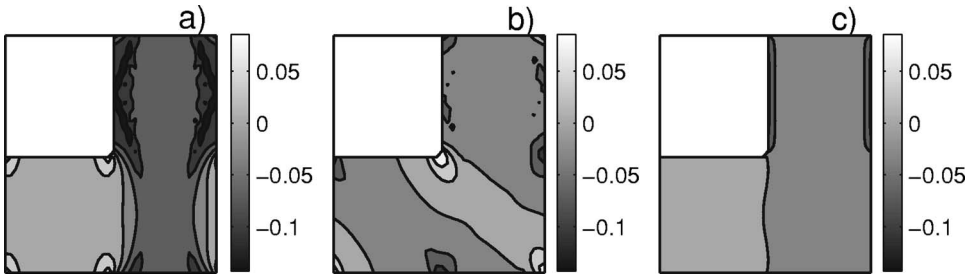

FIG. 5. Demagnetizing field (normalized by M_s) in the direction opposing the external field as produced by the OOMMF simulation described in the text. (a) is the 120-nm film with $\eta=0°$, (b) is the 120-nm film with $\eta=45°$, and (c) is the 15-nm film with $\eta=0°$.

of the demagnetizing field has been observed in circular permalloy antidot arrays.[16] As $\eta \rightarrow 45°$, the field becomes negative over almost all of the unit cell, as shown in Fig. 5(b). The asymmetry in the demagnetizing field at $\eta = 45°$ is caused by the initial state of the magnetization in the simulation.

In order to model the measured spectra, we assume, as a starting point, that the modes in each principal region (i.e., a region of near constant demagnetizing field) of the structure *do not* interact. The spectrum is then simulated by summing independently the contributions to the total spin-wave spectrum of each micromagnetic computational cell, using the effective frequency corresponding to the local magnetization direction and the demagnetizing field at the cell position. The magneto-optic scattering cross section of each mode was assumed to be equal to that of the corresponding continuous film mode. The spectra were then rescaled to allow comparison with experimental data. These spectra are plotted in Fig. 3 below the experimental spectra for the patterned films.

IV. DISCUSSION

Examination of Fig. 3 shows that the model spectra closely resemble the experimental spectra. The splitting is replicated in both the surface and volume modes. The model also reproduces the decrease in the magnitude of the splitting with decreasing film thickness and replicates the collapse in the splitting as $\eta \rightarrow 45°$. The close match implies that *in these structures*, the spin-wave behavior is dominated by the effect of the demagnetizing field rather than the boundary conditions at the edges of the pattern; i.e., to understand the spin-wave mode properties we must take into account the effect of the structure on the demagnetizing field but need not explicitly consider the effect of the boundary conditions on the spin-wave function at the edges of the pattern. A similar result has also been reported for spin waves in small magnetic particles.[17,18]

Regions near stationary points in the demagnetizing field contribute a large intensity at nearly the same spin-wave frequency. Thus the bimodal splitting seen in the spectra may be explained by a demagnetizing field map with two dominant regions. Figure 5(a) shows this to be the case: the large region around Q gives rise to a peak above the continuous film frequency and the smaller uniform regions around P and R combine to produce a peak below the continuous film frequency.

Comparison of Figs. 5(a) and 5(c) shows that the difference in the demagnetizing field between Q and P/R is greater for the 120-nm structure than for the 15-nm structure resulting in a measurable peak splitting. This is simply caused by the larger surface area over which $\nabla \cdot \mathbf{M} \neq 0$ in the thicker film. Hence the splitting is expected to be dependent on the sample thickness, as observed.

We can now explain the collapse of the splitting shown in Fig. 4: as $\eta \rightarrow 45°$ the positive demagnetizing field at Q is replaced by a negative demagnetizing field throughout the unit cell [Fig. 5(b)] and the high-frequency mode moves down in frequency until it merges with the lower-frequency mode [Fig. 4(b)]. The model also correctly predicts the greater splitting for the volume modes. Such an enhancement is consistent with the stronger field dependence of the volume mode compared to the surface mode. This is illustrated in Fig. 2; the total fields at Q and R are indicated by the vertical dotted lines (the vertical solid line represents the external field).

Considering the lateral coherence of the spin-wave modes of the array, it is noteworthy that despite the extended nature of the antidot structure, two distinct surface and first volume mode frequencies coexist, respectively. Our model implies that, if two nearby points in the structure have a demagnetizing field that is sufficiently different so that their resonant frequencies differ by more than the natural linewidth of the material (of the order of 300 MHz for $Ni_{80}Fe_{20}$, Ref. 19), the spin waves at those points appear to be uncoupled. Given that the exchange coupling is unbroken throughout the extended structure *and* that the spin-wave coherence length (for the corresponding continuous films) extends over several unit-cell lengths, it is, at first sight, surprising that a split mode spectrum is observed since for strong coupling a coupled mode behavior might be expected. In contrast, the independent dominant modes survive and must correspond to the spin waves propagating across several unit cells. We therefore conclude that there is only weak coupling between the principal modes.

V. CONCLUSIONS

We have shown that both the surface and volume spin-wave modes are split in a square antidot film, and that this splitting collapses as the external field moves away from a principal axis of the array. We have successfully explained this behavior by modeling the demagnetizing field and the measured spin-wave spectra. We conclude that the local modulation of the demagnetizing field present in the antidot structures principally determines the spin-wave spectra. The edge boundary conditions are found to have no influence on the spin waves in contrast to the observations of confinement reported for isolated structures (rectangles, dots).

ACKNOWLEDGMENTS

We would like to acknowledge the financial support of the EPSRC. One of us (S.Mc.) gratefully acknowledges the financial support of Seagate Technology Ltd. We would also like to thank Dr. Nick Appleyard and Dr. S. J. Steinmüller for several useful discussions.

[1] G. J. Tarnopolsky, D. Q. Chen, M. L. Covault, M. Fallis, S. Gangopadhyay, S. D. Harkness, J. K. Price, R. Y. Ranjan, G. C. Rauch, H. J. Richter, K. Subramanian, E. Y. Yan, and Z. Zhang, IEEE Trans. Magn. **36**, 73 (2000).
[2] R. W. Damon and J. R. Eshbach, J. Phys. Chem. Solids **19**, 308 (1961).
[3] C. E. Patton, Phys. Rep. **103**, 251 (1984).
[4] R. J. Hicken, D. E. P. Eley, M. Gester, S. J. Gray, C. Daboo, A. J. R. Ives, and J. A. C. Bland, J. Magn. Magn. Mater. **145**, 278 (1995).
[5] B. A. Gurney, P. Baumgart, V. Speriosu, R. Fontana, A. Patlac, T. Logan, and P. Humbert, *Proceedings of the International Conference on Magnetic Films and Surfaces, Glasgow 1991* (IoP, London, 1991), P7.12, p. 474.
[6] C. Mathieu, J. Jorzick, A. Frank, S. O. Demokritov, A. N. Slavin, B. Hillebrands, B. Bartenlian, C. Chappert, D. Decanini, F. Rousseaux, and E. Cambril, Phys. Rev. Lett. **81**, 3968 (1998).
[7] J. Jorzick, S. O. Demokritov, B. Hillebrands, B. Bartenlian, C. Chappert, D. Decanini, F. Rousseaux, and E. Cambril, J. Appl. Phys. **87**, 5082 (2000).
[8] J. Jorzick, S. O. Demokritov, B. Hillebrands, M. Bailleul, C. Fermon, K. Y. Guslienko, A. N. Slavin, D. V. Berkov, and N. L. Gorn, Phys. Rev. Lett. **88**, 047204 (2002).
[9] G. Gubbiotti, G. Carlotti, T. Okuno, T. Shinjo, F. Nissoli, and R. Zivieri, Phys. Rev. B **68**, 184409 (2003).
[10] S. O. Demokritov and B. Hillebrands, J. Magn. Magn. Mater. **200**, 706 (1999).
[11] P. Vavassori, V. Metlushko, R. M. Osgood III, M. Grimsditch, U. Welp, G. Crabtree, W. Fan, S. R. J. Brueck, B. Ilic, and P. J. Hesketh, Phys. Rev. B **59**, 6337 (1999).
[12] I. Guedes, V. Metlushko, N. J. Zaluzec, M. Grimsditch, P. Vavassori, B. Ilic, P. Neuzil, and R. Kumar, Phys. Rev. B **62**, 11 719 (2000).
[13] M. Grimsditch, I. Guedes, P. Vavassori, V. Metlushko, B. Ilic, P. Neusil, and R. Kumar, J. Appl. Phys. **89**, 7096 (2001).
[14] R. Zivieri, P. Vavassori, L. Giovannini, F. Nizzoli, E. E. Fullerton, M. Grimsditch, and V. Metlushko, Phys. Rev. B **65**, 165406 (2002).
[15] The OOMMF modeling package is available from http://math.nist.gov/oommf/
[16] C. Yu, M. J. Pechan, and G. J. Mankey, Appl. Phys. Lett. **83**, 3948 (2003).
[17] K. Y. Guslienko, S. O. Demokritov, B. Hillebrands, and A. N. Slavin, Phys. Rev. B **66**, 132402 (2002).
[18] M. Grimsditch, G. K. Leaf, H. G. Kaper, D. A. Karpeev, and R. E. Camley, Phys. Rev. B **69**, 174428 (2004).
[19] J. Dubowik, F. Stobiecki, and T. Luciński, Phys. Rev. B **57**, 5955 (1998).